

Numerical modeling of two-fluid Taylor–Couette flow with deformable capillary liquid–liquid interface

Alexander Yu. Gelfgat

School of Mechanical Engineering, Faculty of Engineering, Tel-Aviv University, Ramat Aviv, Tel Aviv 69978, Israel

Alexander L. Yarin and Pinhas Z. Bar-Yoseph

Faculty of Mechanical Engineering, Technion—Israel Institute of Technology, Haifa 32000, Israel

Michael D. Graham and Guiyu Bai

Department of Chemical and Biological Engineering, University of Wisconsin-Madison, Madison, Wisconsin 53706-1691

(Received 24 September 2003; accepted 20 July 2004; published online 5 October 2004)

A two-fluid Taylor–Couette flow with a deformable interface separating two liquid layers is studied numerically by a combination of the finite volume and level set methods. Effect of the interfacial tension is accounted for. It is shown that if the layers are infinitely long, there exist stable steady states with Taylor vortices of finite strength and finite deformations of the interface. On the other hand, if the length of the layers is finite and no-slip conditions are imposed at the edges, the liquid–liquid interface becomes unstable near the edges. Data from the literature and experimental data acquired in the present work are used for comparison with the numerical predictions. A qualitative agreement between the experimental and numerical observations of this instability is obtained. The results are of potential importance for development of bioseparators employing Taylor vortices for enhancement of mass transfer of a passive scalar (say, a protein) through the interface. © 2004 American Institute of Physics. [DOI: 10.1063/1.1791171]

I. INTRODUCTION

The present study is focused on the numerical modeling of deformations of a liquid–liquid interface in a two-fluid Taylor–Couette apparatus. The study is motivated by recent experiments,^{1,2} whose purpose was to build a novel bioreactor/bioseparator using the Taylor vortices for enhancement of mass transfer through the liquid–liquid interface. A possibility of such an enhancement was demonstrated experimentally^{1,2} and theoretically.^{3,4} One of the main difficulties in the establishing and sustaining the two-fluid Taylor–Couette vortical flow reported in Refs. 1 and 2 was related to the instability of the liquid–liquid interface occurring near the edges of the rotating cylinders.

In the present study temporal development of a perturbed liquid–liquid interface in the Couette–Taylor apparatus is modeled using the finite volume method for calculation of the flow and the level set method⁵ for tracking of the deformable boundary between the layers. It is assumed that the space between two independently rotating cylinders is filled by two immiscible incompressible Newtonian fluids, so that each fluid forms a cylindrical layer adjacent to one of the cylinders (Fig. 1). Beyond the critical Reynolds number a system of Taylor vortices develops in each of the layers. Linear stability and emerging of the Taylor vortices in such a system were studied for nondeformable^{6,7} and for deformable^{8,9} liquid–liquid interfaces. The purpose of the present study is calculation of a supercritical Taylor–Couette flow with vortices in the two layers accounting for possible deformations of the liquid–liquid interface. Interfacial tension is accounted for.

Regarding the bioseparator design mentioned above, we are interested to find a set of parameters providing a stable and steady Taylor–Couette flow, with rather intensive vortices and not very large deformations of the interface. Calculations of the time evolution of the flow and the interface show that it, indeed, approaches the desirable structure when the axially periodic boundary conditions are imposed. This corresponds to the case of infinitely long cylindrical layers, which does not fully represent the relevant experimental setup.¹

On the other hand, when the layers are finite and no-slip conditions are applied at the edges, the time evolution of the liquid–liquid interface does not approach any steady state. The interface deforms strongly tending to reach one of the cylindrical boundaries. Consideration of rather long, but finite, cylindrical layers shows that in the central part of the system the interface behaves similarly to the infinite layer case. However, it exhibits an unstable behavior near the edges. This interfacial instability as well as an enlargement of the Taylor vortices near the edges agree qualitatively with the experimental observations.^{1,2} A large number of the governing parameters of the flow does not allow us to perform a detailed parametric investigation of this instability. Based on the examples considered, it is concluded that the liquid–liquid interface is unstable in Taylor–Couette apparatuses of finite length, which makes it difficult to perform protein separation for a sufficiently long time.

The problem is posed in Sec. II, where the numerical technique is also discussed. The numerical results are discussed and compared to the data found in literature in Sec.

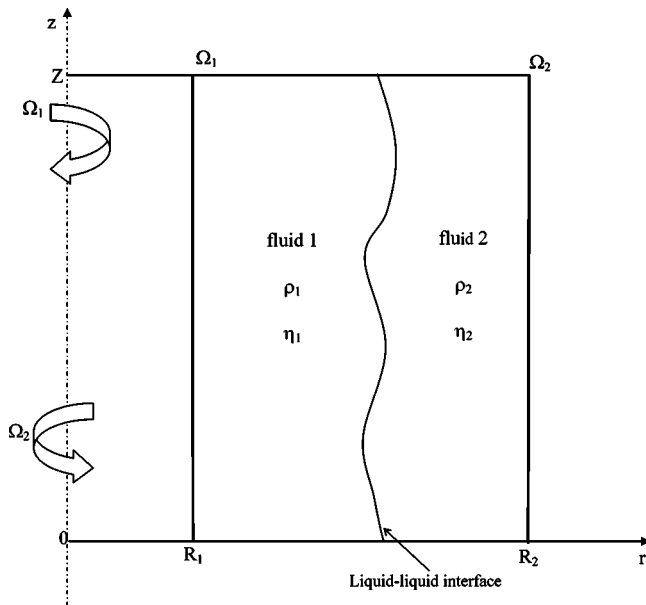


FIG. 1. Sketch of the problem.

III A. In Sec. III B the experiments conducted in the present work are described and the data obtained are compared with the calculations. Conclusions are derived in Sec. IV.

II. FORMULATION OF THE PROBLEM AND NUMERICAL TECHNIQUE

Consider a two-layer Taylor–Couette system shown schematically in Fig. 1. The inner and outer fluid layers are attached to the corresponding cylinders which can rotate independently with angular velocities Ω_1 and Ω_2 , respectively. Both fluids are Newtonian and isothermal. The interface separating the two fluids is assumed to be deformable with the capillary force acting on it. Following the two-fluid model defined in Refs. 1, 10, and 11, the flow in both layers is described by the momentum equation with the volumetric representation of the capillary force,¹²

$$\rho \left[\frac{\partial \mathbf{v}}{\partial t} + (\mathbf{v} \cdot \nabla) \mathbf{v} \right] = -\nabla p + \nabla \cdot (2\mu \mathbf{D}) + \gamma \kappa \delta(\phi) \mathbf{n}, \tag{1}$$

and the continuity equation

$$\nabla \cdot \mathbf{v} = 0. \tag{2}$$

Here $\mathbf{v}=(u,v,w)$ is the flow velocity, p is the pressure, ρ is the density, μ is the dynamic viscosity, \mathbf{D} is the rate-of-strain tensor, γ is the surface tension coefficient, $\kappa=(\nabla \cdot \mathbf{n})$ is the curvature of the liquid–liquid interface, δ is the Dirac delta function, and $d=|\phi|$ and \mathbf{n} are the normal distances reckoned from the deformed interface and the unit outward normal to the liquid–liquid interface. The density and viscosity are equal to ρ_1 and μ_1 in liquid 1 and ρ_2 and μ_2 in liquid 2. The three components of velocity and the pressure are assumed to be axisymmetric. The centrifugal acceleration, which can be estimated as $\Omega^2 R$, reaches at the experimental values of $\Omega = 10 \text{ rpm} = 62.8 \text{ 1/s}$ and $R = 10 \text{ cm}$ the value of 394.4 m/s^2 , which is much larger than the gravity acceleration

9.81 m/s^2 . Therefore the gravity effect is neglected.

The interface is defined by the position of zero level of the level set function ϕ . This function is defined as the signed distance to the liquid–liquid interface, namely,

$$\phi = \begin{cases} -d, & \text{in liquid 1} \\ 0, & \text{on the interface} \\ d, & \text{in liquid 2} \end{cases}. \tag{3}$$

The curvature and the unit normal are derived from Eq. (3) as⁵

$$\mathbf{n} = \nabla \phi / |\nabla \phi|, \quad \kappa = \nabla \cdot \mathbf{n}. \tag{4}$$

At each time moment the level set function is obtained as a solution of the equation

$$\frac{\partial \phi}{\partial t} + (\mathbf{v} \cdot \nabla) \phi = 0, \tag{5}$$

so that the zero level of ϕ moves together with the liquid–liquid interface.⁵

The length, time, velocity, and pressure in Eqs. (1) and (2) are rendered dimensionless by $l=R_2-R_1$, $l/R_1\Omega_1$, $\Omega_1 R_1$, and $(\Omega_1 R_1)^2 \rho_1$, respectively. After the nondimensionalization Eq. (1) reads

$$\rho \left[\frac{\partial \mathbf{v}}{\partial t} + (\mathbf{v} \cdot \nabla) \mathbf{v} \right] = -\nabla p + \frac{1}{\text{Re}} \nabla \cdot (2\mu \mathbf{D}) + \text{We}^{-1} \delta(\phi) \frac{\nabla \phi}{|\nabla \phi|} \cdot \left(\frac{\nabla \phi}{|\nabla \phi|} \right), \tag{6}$$

where $\text{Re}=\Omega_1 R_1 l \rho_1 / \mu_1$ is the Reynolds number and $\text{We}^{-1} = \gamma / (l \Omega_1^2 R_1^2 \rho_1)$ is the reciprocal Weber number. The dimensionless density and viscosity in (6) are defined as

$$\rho = \rho_{21} H(\phi) + [1 - H(\phi)], \tag{7}$$

$$\mu = \mu_{21} H(\phi) + [1 - H(\phi)], \tag{8}$$

where $H(\phi)$ is the step Heaviside function and $\rho_{21}=\rho_2/\rho_1$ and $\mu_{21}=\mu_2/\mu_1$ are the density and dynamic viscosity ratios, respectively.

The problem is considered in the domain $R_1/l \leq r \leq R_2/l$, $0 \leq z \leq A$, $A=Z/l$ (see Fig. 1) with no-slip boundary conditions at $r=R_1/l$ and $r=R_2/l$:

$$r = R_1/l: u = w = 0, v = 1, \tag{9}$$

$$r = R_2/l: u = w = 0, v = \Omega_{21} R_{21}, \tag{10}$$

where $\Omega_{21}=\Omega_2/\Omega_1$ and $R_{21}=1/R_{12}=R_2/R_1$ are the angular velocities and the radii ratios, respectively. On the boundaries $z=0$ and $z=A$ we consider either periodicity conditions

$$\mathbf{v}(z=0) = \mathbf{v}(z=A), \quad p(z=0) = p(z=A), \tag{11}$$

or no-slip conditions

$$z = 0 \text{ and } z = A: u = w = 0, \quad v = \Omega_z r / R_1, \tag{12}$$

where $\Omega_z=1$ (the boundaries rotate with the inner cylinder) or $\Omega_z=\Omega_{21}$ (the boundaries rotate with the outer cylinder).

The numerical implementation of Eqs. (6)–(8) requires a smoothing of the δ and Heaviside functions in the vicinity of the liquid–liquid interface (i.e., in the vicinity of the zero level set). These functions are smoothed as proposed in Ref. 13,

$$\delta_\varepsilon(x) = \begin{cases} \frac{1}{2\varepsilon} \left[1 + \cos\left(\frac{\pi x}{\varepsilon}\right) \right] & \text{if } |x| < \varepsilon, \\ 0, & \text{otherwise,} \end{cases} \quad (13)$$

$$H_\varepsilon(x) = \begin{cases} 0 & \text{if } x < -\varepsilon, \\ \frac{x + \varepsilon}{2\varepsilon} + \frac{1}{2\pi} \sin\left(\frac{\pi x}{\varepsilon}\right) & \text{if } |x| \leq \varepsilon, \\ 1 & \text{if } x > \varepsilon, \end{cases} \quad (14)$$

where $\varepsilon \ll 1$.

The problem is solved numerically using the finite volume discretization of Eq. (6) on the staggered and uniform grid. The small parameter ε in Eqs. (13) and (14) was taken in Ref. 11 to be 2.5 times the mesh size. Since in the present case the number of grid nodes can change in r and z directions independently, we define $\varepsilon = 2\sqrt{h_r^2 + h_z^2}$ which yields a close value of $2.83h_r$ for equal mesh sizes $h_r = h_z$ in radial and axial directions. Solution of Eqs. (2) and (6) is carried out using the semi-implicit method for pressure-linked equations (SIMPLE) algorithm¹⁴ for time integration. Equation (5) is discretized in space using the second-order essentially non-oscillatory (ENO) scheme.¹¹ Each time step of Eq. (5) requires a reinitialization procedure for ϕ to restore its property of the signed distance for the liquid–liquid interface. We use the same reinitialization procedure as in Refs. 10, 11, and 15, which requires numerical integration of the problem

$$\frac{\partial \phi}{\partial \tau} + \text{sgn}(\phi_0)(|\nabla \phi| - 1) = 0, \quad \phi(\tau = 0) = \phi_0, \quad (15)$$

up to the convergence. Here ϕ_0 is the level set function obtained after a single time step integration of Eq. (5) and $\text{sgn}(x) = 2H(x) - 1$ is the signum function. Equation (15) is discretized in space using the third-order ENO scheme.¹⁶ The time integration of Eq. (15) is followed by the volume-correction procedure proposed in Ref. 17. With these procedures we observe that the deviation of the volume remains within 1%. For a better efficiency the convergence of Eq. (15) is required within a tube whose boundaries are located at approximately 10 mesh layers from the curve $\phi_0 = 0$.¹⁸ The calculations always started from the perturbed Couette flow. An initial perturbation proposed in Ref. 19, which allows for triggering the onset of Taylor vortices, was extended to the two-layer case. The liquid–liquid interface was also perturbed using a $2\pi/Z$ -periodic cosine function multiplied by a small amplitude. The time step was calculated as in Ref. 10. An example of the convergence study is described in the Appendix.

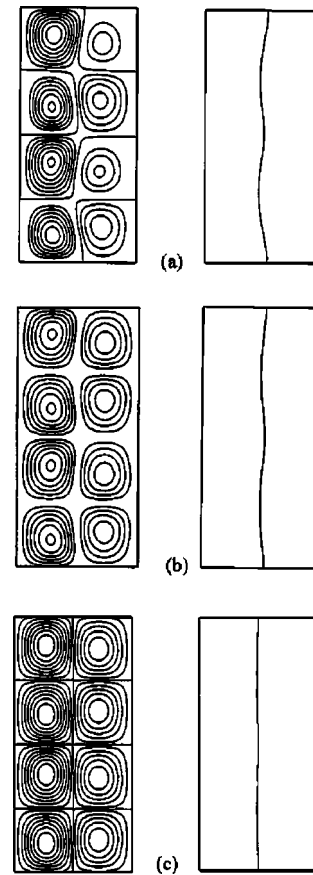


FIG. 2. Streamlines (the left frames) and position of the interface (the right frames) of steady flows calculated for axially periodic boundary conditions. A wide gap $R_{12}=0.5$, $A=2$, $We^{-1}=0.01$, $Re=500$, (a) $\Omega_{21}=0$, (b) $\Omega_{21}=0.1$, (c) $\Omega_{21}=0.2$.

III. RESULTS

A. Numerical modeling

To estimate the reciprocal Weber number We^{-1} we refer to the recent experiment,¹ from which we take roughly $R_1 \sim 0.05$ m, $l \sim 0.005$ m, $\Omega_1 \sim 10$ Hz, and $\rho_1 \sim 800$ kg m⁻³. The surface tension between the two liquid phases usually is not known. We estimate it to be $\gamma \sim 10^{-2}$ N m⁻¹, of the order of the surface tension at water–air interface. This yields the value $We^{-1} \approx 0.01$, which was used in the calculations described below. The density and viscosity ratios were chosen as $\rho_{12}=1.4$ and $\eta_{12}=0.96$, respectively, which correspond to one of the experiments in Ref. 1.

The first series of the calculations was performed for the axially periodic boundary conditions (11) for the pressure and velocity field. Periodicity conditions are also imposed on the level set function ϕ . A wide-gap case with $R_{12}=0.5$ and $A=2$ was considered as a primary example, not directly related to the experiments described below. The result is shown in Fig. 2. This case was chosen because the Taylor vortices in this case appear at relatively small Reynolds number, $Re \approx 100$. To allow for a significant strength of the vortices larger Reynolds numbers, $Re=300$ or 500 , were used in the calculations. The flow with $\Omega_{21}=0$ and prescribed nondeformable liquid–liquid interface was calculated first. Then the interface was perturbed (with the amplitude of 1% of its

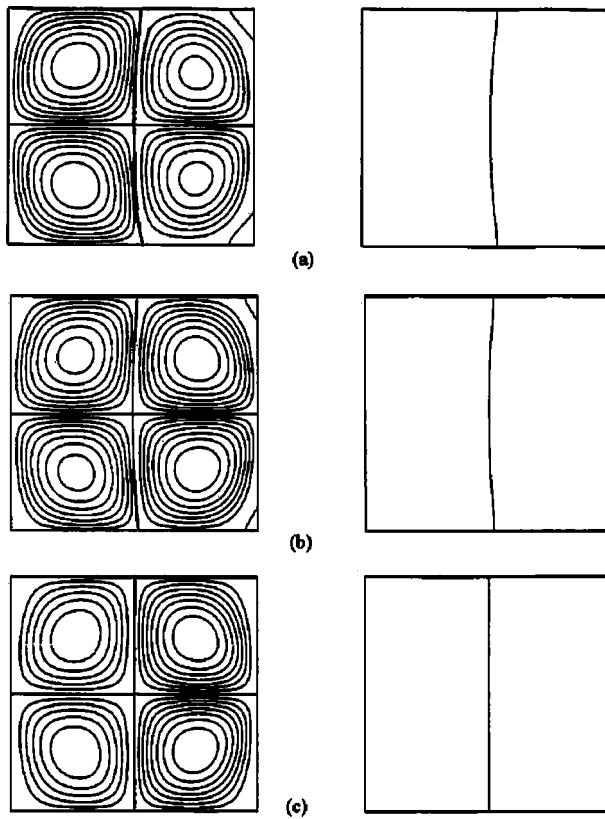


FIG. 3. Streamlines (the left frames) and position of the interface (the right frames) of steady flows calculated for axially periodic boundary conditions. Narrow gap $R_{12}=0.827$, $A=1$, $We^{-1}=0.01$, $Re=4490$. (a) $\Omega_{21}=-0.2$, (b) $\Omega_{21}=0.2$, (c) $\Omega_{21}=0.62$.

radius) and straightforward integration in time was carried out until the flow reached the steady state shown in Fig. 2(a) for $\Omega_{21}=0$. The next result for $\Omega_{21}=0.1$ [Fig. 2(b)] was calculated using the previous result as an initial guess. In the

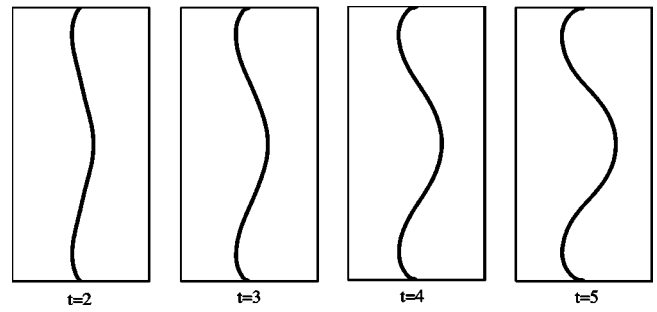


FIG. 4. Position of the liquid–liquid interface at several successive time moments. Calculation for motionless ends of the interface. $R_{12}=0.5$, $A=2$, $We^{-1}=0.01$, $Re=300$, $\Omega_{21}=0$. Calculations started from a developed Taylor–Couette vortical flow and undeformed interface.

same way the result for $\Omega_{21}=0.2$ [Fig. 2(c)] was obtained starting from the steady state at $\Omega_{21}=0.1$. Figure 2 shows that corotation of the cylinders smoothens the liquid–liquid interface if the periodic boundary conditions are imposed. All the calculations were carried out on the 50×100 uniform grid.

Calculations for a narrow gap $R_{12}=0.827$, corresponding to the experiment,¹ show a similar behavior of the interface (Fig. 3). Here the deformations of the interface are smaller because of the narrower gap and larger Reynolds number, both of which lead to larger pressure gradients on both sides of the interface. The interface is almost straight at the experimental value of the rotation ratio¹ $\Omega_{21}=0.62$, which agrees with the experimental observations at short times. This series of calculations was performed on the 100×100 uniform grid.

When the no-slip boundary conditions (12) are applied, the boundary conditions at $z=0, A$ for the level set function

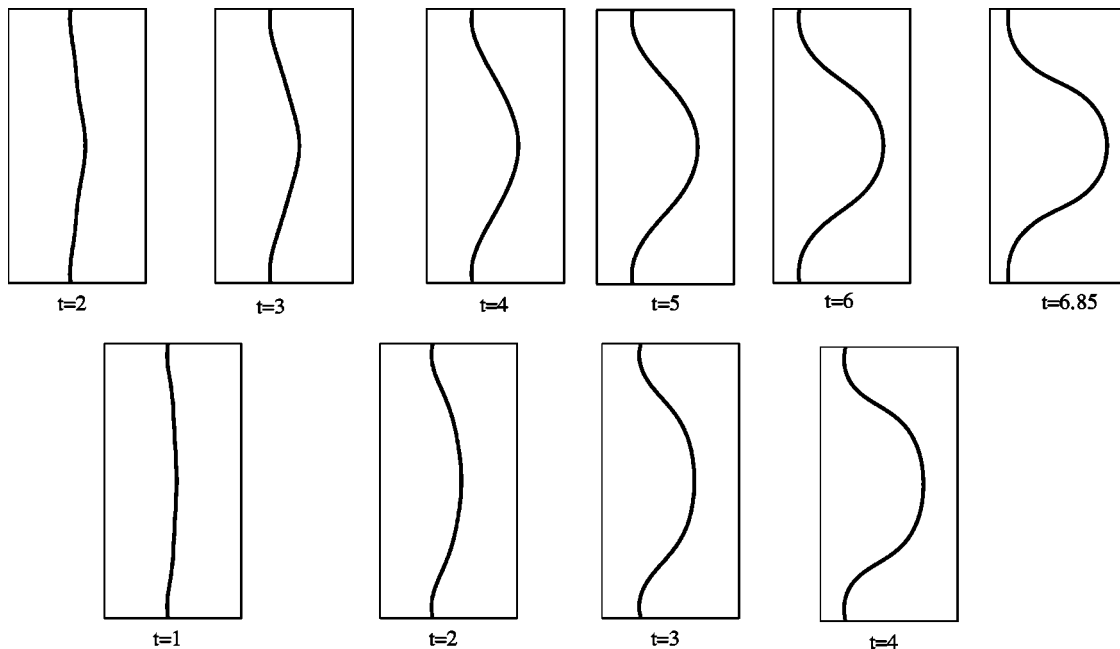


FIG. 5. Position of the liquid–liquid interface at several successive time moments. Calculation with the contact angle of 90° . $R_{12}=0.5$, $A=2$, $We^{-1}=0.01$, $Re=300$. Upper frames: $\Omega_{21}=0$, lower frames: $\Omega_{21}=0.5$.

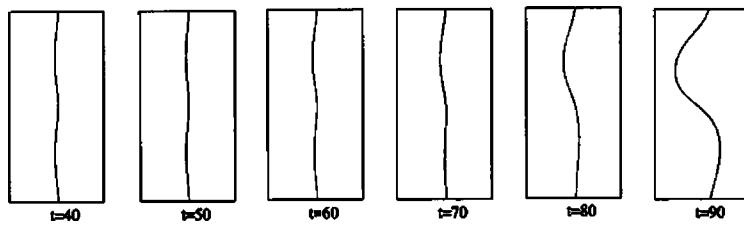


FIG. 6. Position of the liquid–liquid interface at several successive time moments. Calculation with the contact angle of 90° . $R_{12}=0.5$, $A=2$, $We^{-1}=0.01$, $Re=500$, $\Omega_{21}=0.1$, $\rho_{12}=\eta_{12}=1$.

are not obvious. In the case of axisymmetric interface the formal extension of Eq. (5) to the boundaries yields

$$\frac{\partial \phi}{\partial t} = 0 \text{ at } z=0, A, \quad (16)$$

which means that the “ends” of the interface are motionless. An example of the calculations with these boundary conditions is shown in Fig. 4. The calculations started from a developed Taylor–Couette vortical flow at $Re=300$ and an undeformable interface. After the interface was slightly perturbed, its evolution (see Fig. 4) led to strong deformations until the interface reached the middle of the outer boundary.

The boundary conditions (16) contradict the usually imposed conditions of a static or dynamic contact angle (the latter is a function of the velocity of the contact line). The conditions for the contact angle would define the spatial derivatives of the level set function rather than its temporal derivative in Eq. (16). Moreover, since the wettability effects in the present case are expected to be much weaker than the bulk flow, the influence of a certain value of the dynamic contact angle on the general flow structure is expected to be negligible.^{20–22} Since wettability of the experimental liquids at the container top/bottom is unknown, an arbitrary contact

angle of 90° was used in further calculations. This leads to the Neumann-type boundary condition for the level set function, namely,

$$\frac{\partial \phi}{\partial z} = 0 \text{ at } z=0, A, \quad (17)$$

and allows calculation from an unperturbed interface state. Calculations with this boundary also do not reach a steady position of the interface. This is depicted in Fig. 5, which was obtained for the case $\Omega_z=l/R_{21}$, i.e., the upper and lower boundaries moving together with the outer cylinder. A similar result was also obtained when these boundaries moved together with the inner cylinder, $\Omega_z=1$. Note that in this case the corotation did not stabilize or smooth the interface, as it was observed for the periodic boundary conditions (Figs. 2 and 3). Moreover, corotation even enhanced the interface deformation.

A series of calculations for different values of the rotation, density, and viscosity ratios were carried out to find a case for which the liquid–liquid interface would approach a stable steady state with no-slip boundary conditions at $z=0, A$. However, in all the cases considered the interface deformed and reached one of the cylindrical boundaries. Figure 6 illustrates the case of $\rho_{12}=\eta_{12}=1$, for which the longest

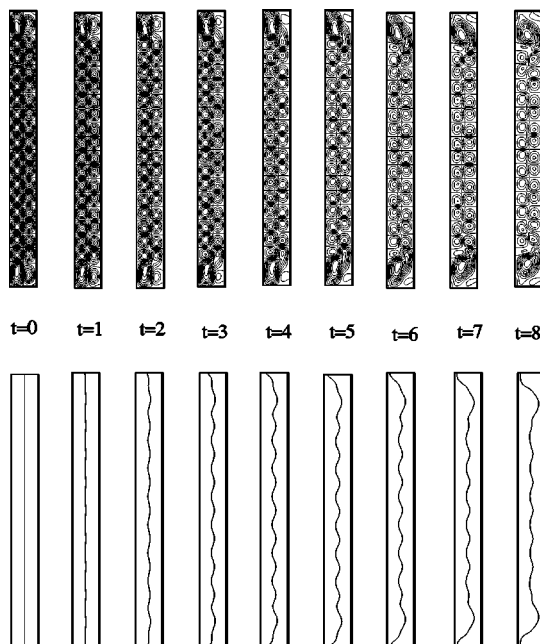


FIG. 7. Streamlines (the upper frames) and position of the liquid–liquid interface (the lower frames) at several sequential time moments. $R_{12}=0.5$, $A=10$, $We^{-1}=0.01$, $Re=500$, $\Omega_{21}=0$.

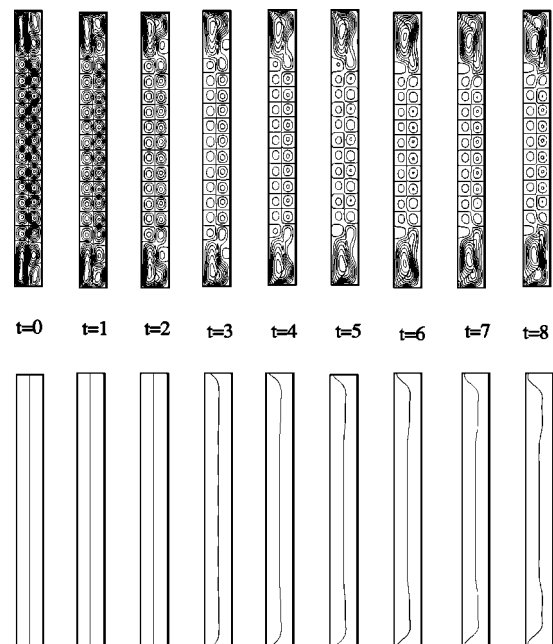


FIG. 8. Streamlines (the upper frames) and position of the liquid–liquid interface (the lower frames) at several sequential time moments. $R_{12}=0.5$, $A=10$, $We^{-1}=0.01$, $Re=500$, $\Omega_{21}=0.2$.

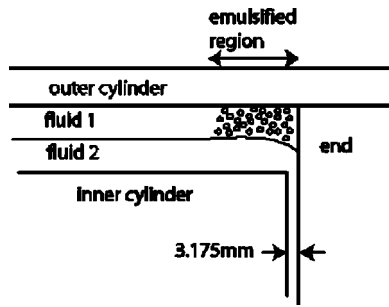


FIG. 9. Sketch of the end region of the experimental setup.

time to observe a visible instability of the interface is required. Such a long time necessary for development of the instability is probably explained by the absence of the jumps of pressure and viscous stresses over the interface. It is also seen that in spite of the fact that the level set function at the boundary nodes at $z=0, A$ is equal to its values at the neighboring nodes, which is the numerical representation of Eq. (17), the flow tends to distort the 90° contact angle. This probably manifests the fact that the boundary conditions implying dynamic contact angle could be needed.

To verify that the observed instability of the liquid–liquid interface is caused by the end effects, a longer flow region with $A=10$ was considered. The calculations were carried out on the 50×200 uniform grid. The boundaries at $z=0, A$ rotated together with the outer cylinder. The results corresponding to two different rotation ratios are shown in Figs. 7 and 8. In both cases we observe a regular vortical structure and regular oscillations of the interface in the central part of the cylindrical layer. At the same time larger vortices and large deformations of the interface develop near the no-slip ends at $z=0, A$. This indicates that the instability of the interface sets in near the no-slip boundaries. A similar result was obtained when the reciprocal Weber number was increased to 0.1, i.e., the interfacial tension was increased. Note that the corotation of the cylinders smooths the interface (cf. Figs. 7 and 8) similarly to what has been observed for shorter domains with the periodic boundary conditions (Figs. 2 and 3). Note also that the development of larger vortices and large deformations of the interface near the no-slip ends were also observed in the experiments.^{1,2} Therefore, in spite of the unknown dynamic contact angle in the

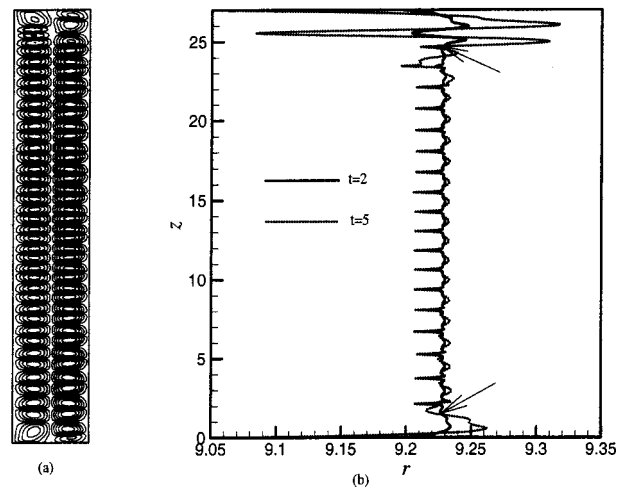


FIG. 10. (a) Streamlines (the radial coordinate is stretched 45 times). (b) Interface configuration at two sequential time moments (the radial coordinate is stretched in 120 times). $R_{12}=0.897$, $A=27$, $We^{-1}=1.5 \times 10^{-3}$, $Re=1550$, $\Omega_{21}=0.5$.

experiments, a qualitatively similar behavior of the liquid–liquid interface near the no-slip edges was predicted theoretically with the contact angle of 90° .

B. Comparison with experiment

Important experiments with the model two-fluid Taylor–Couette bioseparator¹ were conducted in the present work to acquire more data for comparison with the present calculations. The experimental setup has the following parameters: the lengths of the cylinders are 28 cm, the diameters of the inner and the outer cylinders are 9.06 cm and 10.098 cm, respectively, the rotation of the inner cylinder is at 10 rps, the rotation of the outer cylinder varies between 5 and 10 rps, the dynamic viscosities and densities of the inner (50% drakeol+50% isopar) and outer (60% glycerol +40% water) fluids are 7.83 cP, 820 kg m⁻³ and 7.56 cP, 1150 kg m⁻³, respectively. This results in the following values of the dimensionless parameters: the radii ratio $R_{12}=0.8972$, the aspect ratio $A=Z/l=54$, the Reynolds number $Re \approx 1550$, and the rotation ratio varying from $\Omega_{21}=0.5$ to $\Omega_{21}=0.8$. The no-slip end boundaries rotate together with the outer cylinder. The interfacial tension between the fluids is estimated as 0.05 N/m, which yields the inverse Weber

TABLE I. The distance between the deformed interface and the spacer at the midsurface compared with the experimental measurements.

Ω_{out}/Ω_{in}	Distance between the end region close to the left spacer in centimeter at time t		Distance between the end region close to the right spacer in centimeter at time t		Experimentally measured position of the edge of the end vortex (cm)
	$t=5$ s	$t=10$ s	$t=5$ s	$t=10$ s	
0.5	0.72	1.13	0.61	1.15	1.15
0.6	0.26	1.18	0.36	1.70	1.08
0.7	0.24	0.78	0.24	0.78	0.88
0.8	0.35	0.63	0.35	0.63	0.35

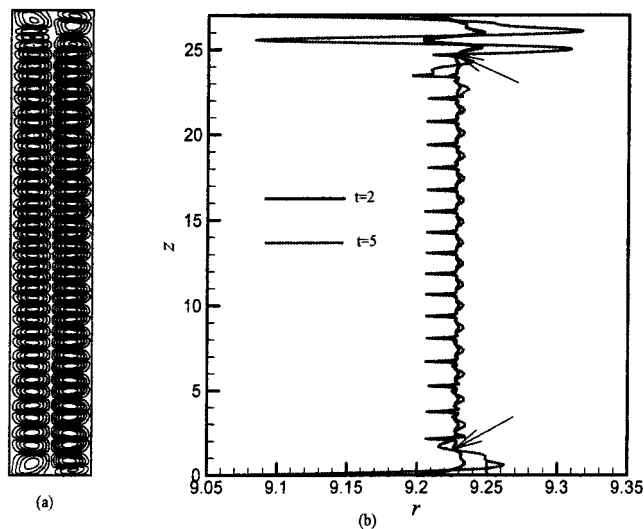


FIG. 11. (a) Streamlines. (b) Interface configuration at two sequential time moments for the boundary conditions (18). $R_{12}=0.897$, $A=27$, $We^{-1}=1.5 \times 10^{-3}$, $Re=1550$, $\Omega_{21}=0.5$.

number $We^{-1} \approx 0.0015$. To reduce the computational costs and assuming that the end effects are already clearly seen at the aspect ratio 10 (cf. Figs. 7 and 8), the calculations were performed at the half of the actual aspect ratio $A=27$. The calculations were done on the uniform grid with 100 and 1000 nodes in the r and z directions, respectively.

The experimental observations of the interface deformations were done in the following way. Consider the schematic of the end region of the experimental setup shown in Fig. 9. It turned out that a weak emulsion was present there at all the outer cylinder rotation rates considered here (except rigid rotation). We took the edge of the region containing emulsion to demarcate the boundary of the end vortex. The computations presented here predict that the interface would actually move down into the narrow gap between the end of the device and the end of the inner cylinder, providing the likely explanation for the origin of the emulsion. The emulsion probably arose from interfacial instability of the two-layer flow due to the very high shear rate in this narrow gap.

An example of the calculated flow is shown in Fig. 10(a) and the interface positions at $t=2$ and 5 are depicted in Fig. 10(b). The boundary conditions (17) for the level set function were imposed. Note that to make the Taylor vortices and the surface deformation visible the radial coordinate is stretched 45 times in Fig. 10(a) and in 120 times in Fig. 10(b). Note

that the dimensionless radial coordinate changes in the interval $8.7276 \approx R_{12}/(1-R_{12}) \leq r \leq 1/(1-R_{12}) \approx 9.7276$, so that the midsurface is located at $r \approx 9.2276$. It is seen that the liquid–liquid interface exhibits the largest deformations near the no-slip end boundaries, which grow in time until the numerical process becomes unstable. Such a behavior of the interface is characteristic of all rotation ratios in the interval $0.5 \leq \Omega_{21} \leq 0.8$. For $\Omega_{21} \geq 0.9$ the Taylor vortices do not develop; therefore these cases were not modeled.

To compare the deformation of the interface near the no-slip boundaries with the experimental observations we estimated the length between these boundaries (the spacers) and the cross sections where regular wiggles of the interface begin. The length was reckoned along the position of the initially undeformed interface. The points used to measure the distance are denoted in Fig. 10(b) by arrows.

Since the numerically estimated length of the end vortices as well as the experimentally measured one are time dependent, only a qualitative comparison of the results is possible. Note also that single fluid Taylor–Couette flows between long but finite cylinders exhibit multiplicity of possible steady states.^{23,24} The multiplicity can be expected also in the present two-fluid case. It was found, for example, that at $\Omega_{21}=0.5$ and 0.6 the flow pattern becomes asymmetric with respect to the axial midplane. This means that a symmetry breaking pitchfork bifurcations takes place somewhere in the interval $0.6 < \Omega_{21} < 0.7$, and there are already two possible steady states at least.

Comparison of the experimental data with the numerical results in Table I shows that for $0.5 < \Omega_{21} < 0.7$ the experimentally measured position of the edge of the end vortex corresponds to the location between the third and the fourth end vortices (the third vortex boundary). The case $\Omega_{21}=0.8$ is different because at this rotation ratio the Taylor vortex structure is not developed yet and only one pair of vortices exists near the end boundaries. A closer look at the evolution of the liquid–liquid interface shows that at $t=10$ the points corresponding to the beginning of the regular interface oscillations (wiggles) are located rather close to the experimentally observed points [see points indicated by arrows in Fig. 10(b)]. This location remains almost unchanged for a rather long time. Thus for $t > 5$ (which corresponds to ≈ 15 s) we observed a rapid growth of the interface deformations near the ends, while deformations at the central part remained almost unchanged.

The calculations were repeated for the conditions of experiments⁶ where the inner part of the end boundary ro-

TABLE II. Convergence of the maximal values of stream function.

Grid $N_r \times N_z$	Without interface deformation		With interface deformation	
	$\psi_{\max}^{\text{inner}}$	$\psi_{\max}^{\text{outer}}$	$\psi_{\max}^{\text{inner}}$	$\psi_{\max}^{\text{outer}}$
30 × 60	0.0307	0.0272	0.0305	0.0299
50 × 100	0.0297	0.0281	0.0296	0.0280
75 × 150	0.0299	0.0279	0.0295	0.0282
100 × 200	0.0298	0.0280	0.0295	0.0281

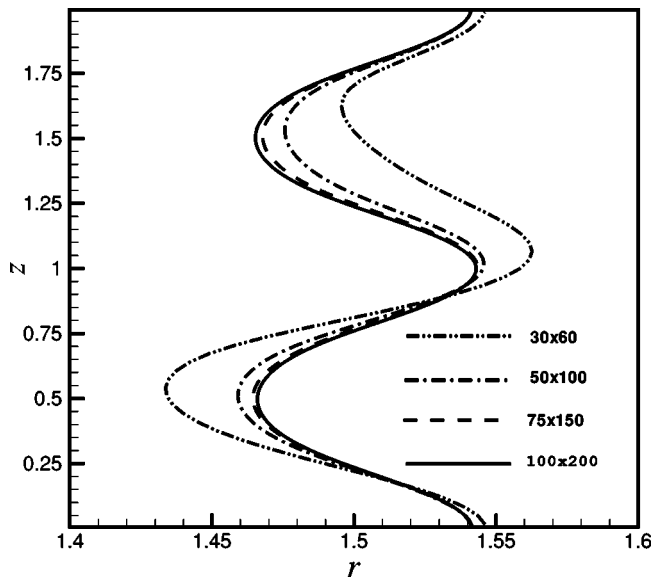


FIG. 12. Position of the interface calculated for axially periodic boundary conditions for different total number of grid points $N_r \times N_z$ (shown on the graph). Radial coordinate is zoomed in ten times. $R_{12}=0.5$, $A=2$, $We^{-1}=0.01$, $Re=500$, $\Omega_{21}=0$.

tated with the inner cylinder and the outer part rotated with the outer one. Thus, instead of (12) we define

$$z=0 \text{ and } z=A: u=w=0, \quad \mathbf{v} = \begin{cases} r\mathbf{l}/R_1, & r \leq \frac{R_1}{l} + \frac{1}{2}, \\ \Omega_{21}r\mathbf{l}/R_1, & r > \frac{R_1}{l} + \frac{1}{2}. \end{cases} \quad (18)$$

The contact line was permitted to move, while the contact angle was fixed at 90° . In this case also the liquid–liquid interface exhibits a behavior similar to that of Fig. 10, which is illustrated in Fig. 11 for $\Omega_{21}=0.5$.

IV. CONCLUSION

It is shown that steady two-fluid Taylor–Couette flow with a deformable capillary liquid–liquid interface can be obtained only in an idealized case of an infinitely long Taylor–Couette apparatus. In the finite length apparatus the interface is found to be unstable near the no-slip edges of the system. It is impossible to conclude that the instability observed retains for all values of the governing parameters, since too many of them are involved. However, the instability was found for all the cases considered. A qualitative agreement between the experimental and numerical results on the instability development was obtained. The instability found is indicative of the extreme difficulties in designing bioseparators/bioreactors based on enhancement of mass transfer by means of the Taylor vortices.

ACKNOWLEDGMENTS

This research was partly supported by BSF (US-Israel Bination Science Foundation) Grant No. 97-118. A.Y.G. was also partly supported by the Center for Absorption in

Science, Israel Ministry of Immigrant Absorption. The authors would like to acknowledge the use of computer resources belonging to the High Performance Computing Unit, a division of the Inter University Computing Center, which is a consortium formed by research universities in Israel.

APPENDIX: AN EXAMPLE OF THE CONVERGENCE STUDY

The convergence of the numerical procedure is illustrated in the case shown in Fig. 2(a). Table II illustrates the convergence of the maximal values of the stream function in the inner and outer liquids. Calculations with and without deformation of the interface are reported. It is seen that the accounting for the interface deformation does not affect the convergence of the flow approximation.

The steady position of the interface calculated with different total number of grid points is shown in Fig. 12. Starting from the mesh with 50 and 100 nodes in the radial and the axial directions, respectively, the calculated interfaces are very close. To illustrate the existing differences the radial coordinate in Fig. 12 was zoomed in 10 times.

- ¹G. Baier, M. D. Graham, and E. N. Lightfoot, "Mass transport in a novel two-fluid Taylor vortex extractor," *AICHE J.* **46**, 2395 (2000).
- ²J. Sato, "Axial dispersion in Taylor–Couette flow," University of Madison–Wisconsin, Report No. 175, 2000.
- ³G. Baier, T. M. Grateful, M. D. Graham, and E. N. Lightfoot, "Prediction of mass transfer rates in spatially periodic flows," *Chem. Eng. Sci.* **54**, 343 (1999).
- ⁴A. L. Yarin, A. Yu. Gelfgat, and P. Z. Bar-Yoseph, "Enhancement of mass transfer in a two-layer Taylor–Couette apparatus with axial flow," *Int. J. Heat Mass Transfer* **45**, 555 (2002).
- ⁵A. Sethian, *Level Set Methods and Fast Marching Methods* (Cambridge University Press, Cambridge, 1999).
- ⁶G. Baier and M. D. Graham, "Two-fluid Taylor–Couette flow: Experiments and linear theory for immiscible liquids between corotating cylinders," *Phys. Fluids* **10**, 3045 (1998).
- ⁷G. Baier and M. D. Graham, "Two-fluid Taylor–Couette flow with counter-current axial flow: Linear theory for immiscible liquids between corotating cylinders," *Phys. Fluids* **12**, 294 (2000).
- ⁸Y. Renardy and D. D. Joseph, "Couette flow of two fluids between concentric cylinders," *J. Fluid Mech.* **150**, 381 (1985).
- ⁹D. D. Joseph, Y. Renardy, M. Renardy, and K. Nguen, "Stability of rigid motions and rollers in bicomponent flows of immiscible liquids," *J. Fluid Mech.* **153**, 151 (1985).
- ¹⁰M. Sussman, P. Smereka, and S. Osher, "A level set approach for computing solutions to incompressible two-phase flow," *J. Comput. Phys.* **114**, 146 (1994).
- ¹¹Y. C. Chang, T. Y. Hou, B. Merriman, and S. Osher, "A level set formulation of Eulerian interface capturing methods for incompressible fluid flows," *J. Comput. Phys.* **124**, 449 (1996).
- ¹²J. U. Brackbill, D. B. Kothe, and C. Zemach, "A continuum method for modeling surface tension," *J. Comput. Phys.* **100**, 335 (1992).
- ¹³C. S. Peskin, "Numerical analysis of blood flow in the heart," *J. Comput. Phys.* **97**, 220 (1977).
- ¹⁴S. Osher and F. P. Fedkiw, "Level set methods: An overview and some recent results," *J. Comput. Phys.* **169**, 463 (2001).
- ¹⁵S. V. Patankar and D. B. Spalding, "A calculation procedure for heat, mass and momentum transfer in three-dimensional parabolic flows," *Int. J. Heat Mass Transfer* **15**, 1787 (1972).
- ¹⁶M. Sussman and E. Fatemi, "An efficient, interface-preserving level set redistancing algorithm and its application to interfacial incompressible fluid flow," *SIAM J. Sci. Comput. (USA)* **20**, 1165 (1999).
- ¹⁷M. Sussman and P. Smereka, "Axisymmetric free boundary problems," *J. Fluid Mech.* **341**, 269 (1997).
- ¹⁸D. Peng, B. Merriman, S. Osher, H. Zhao, and M. Kang, "A PDE-based fast level set method," *J. Comput. Phys.* **155**, 410 (1999).
- ¹⁹W. Schröder and H. B. Keller, "Wavy Taylor-vortex flows via multigrid-

- continuation methods," *J. Comput. Phys.* **91**, 197 (1990).
- ²⁰S. N. Reznik and A. L. Yarin, "Spreading of a viscous drop due to gravity and capillarity on a horizontal or an inclined dry wall," *Phys. Fluids* **14**, 118 (2002).
- ²¹S. N. Reznik and A. L. Yarin, "Strong squeezing flow between parallel plates leads to rolling motion at the contact line," *Int. J. Multiphase Flow* **28**, 911 (2002).
- ²²S. N. Reznik and A. L. Yarin, "Spreading of an axisymmetric viscous drop due to gravity and capillarity on a dry horizontal wall," *Int. J. Multiphase Flow* **28**, 1437 (2002).
- ²³D. Coles, "Transition in circular Couette flow," *J. Fluid Mech.* **21**, 385 (1965).
- ²⁴K. A. Cliffe and T. Mullin, "A numerical and experimental study of anomalous modes in the Taylor experiment," *J. Fluid Mech.* **153**, 243 (1985).